Bipolar corona discharge based air flow generation with low net charge

Article *in* Sensors and Actuators A Physical · April 2016

Impact Factor: 1.9 · DOI: 10.1016/j.sna.2016.03.028

4 authors:

Van Thanh Dau

Sumitomo Chemical

63 PUBLICATIONS **272** CITATIONS

SEE PROFILE

Thien X Dinh

Ritsumeikan University

59 PUBLICATIONS **151** CITATIONS

SEE PROFILE

Tibor Terebessy

16 PUBLICATIONS **75** CITATIONS

SEE PROFILE

Bui Thanh Tung

Vietnam National University, Hanoi

54 PUBLICATIONS **153** CITATIONS

SEE PROFILE

Sensors and Actuators A 244 (2016) 146–155

Contents lists available at ScienceDirect

Sensors and Actuators A: Physical

journal homepage: www.elsevier.com/locate/sna

Bipolar corona discharge based air flow generation with low net charge

Van Thanh Dau [a,*], Thien Xuan Dinh [b], Tibor Terebessy [c], Tung Thanh Bui [d,e]

[a] Research Group (Environmental Health), Sumitomo Chemical Ltd., Hyogo 665-8555, Japan
[b] Graduate School of Science and Engineering, Ritsumeikan University, Shiga 525-8577, Japan
[c] Atrium Innovation Ltd., Lupton Road, OX10 9BT Wallingford, United Kingdom
[d] Nanoelectronics Research Institute, National Institute of Advanced Industrial Science and Technology, Tsukuba 305-8568, Japan
[e] Faculty of Electronics and Telecommunication (FET), University of Engineering and Technology (UET), Vietnam National University, Hanoi (VNUH), Viet Nam

ARTICLE INFO

Article history:
Received 17 January 2016
Received in revised form 4 March 2016
Accepted 27 March 2016
Available online 16 April 2016

Keywords:
Electrohydrodynamic
Neutralized ion wind
OpenFOAM
Bipolar corona discharge
Parallel pin

ABSTRACT

In this paper, we report on a miniaturized device that can generate ion wind flow with very low net charge. Both positive and negative ions are simultaneously generated from two sharp electrodes placed in parallel, connected to a single battery-operated power source. The two-electrode arrangement is symmetrical, where the electrode creating charged ions of one polarity also serves as the reference electrode to establish the electric field required for ion creation by the opposite electrode, and vice versa. The numerical simulation is carried out with programmable open source OpenFOAM, where the measured current-voltage is applied as boundary condition to simulate the electrohydrodynamics flow. The air flow inside the device is verified by eight hotwires embedded alongside the downstream channel. It was confirmed that the jet flow generated in the channel has a linear relationship with the square root of the discharge current and its measured values agree well with simulation. The device is robust, ready-to-use and minimal in cost. These are important features that can contribute to the development of multi-axis fluidic inertial sensors, fluidic amplifiers, gas mixing, coupling and analysis. The proposed configuration is beneficial with space constraints and/or where neutralized discharge process is required, such as inertial fluidic units, circulatory flow heat transfer, electrospun polymer nanofiber to overcome the intrinsic instability of the process, or the formation of low charged aerosol for inhalation and deposition of charge particles.

1. Introduction

Flow is known as a vital aspect in the function of microfluidic devices. Flow generators are essential for any microfluidic system and have been an attractive topic of research for decades [1]. Depending on the working principle, flow generators can be classified into displacement type and dynamic type [2] categories, which distinguishes the reciprocating and the continuous flow [3]. In terms of geometry, an additional classification separates these devices into categories with and without a check-valve, or further classification is based on the design parameters, such as the size, rate, and power density [4]. In parallel with advancements in micro technology, micropumps especially valveless pumps usually cover a hybrid study in conjunction with jet flow generation. This inherently made piezoelectric lead zirconate titanate (PZT) as the most commonly used actuator for valveless displacement type because of its small stroke volumes, large natural frequencies and commercial availability [5–10].

Another way to create jet flow is by electrokinetic actuation. Under a strong electric field, every charged particle is subjected to Coulomb force and while accelerated by the field, the charge particles collide with neutral fluid molecules, transferring momentum which results in fluid drift. The sum of Coulomb forces is called the volumetric electrohydrodynamics (EHD) force. This principle can be applied upon either the existence of space charge in the fluid such as ion injection pumping from corona discharge [11], conduction pumping for weak electrolyte [12], induction pumping for surface charge in a dielectric [13], or Maxwell pressure gradi-

* Corresponding author.
E-mail addresses: dauv@sc.sumitomo-chem.co.jp, dauthanhvan@gmail.com (V.T. Dau), thien@cfd.ritsumei.ac.jp (T.X. Dinh), tibor.terebessy@clearviewtraffic.com (T. Terebessy), tung.bui@aist.go.jp (T.T. Bui).

http://dx.doi.org/10.1016/j.sna.2016.03.028
0924-4247/

Nomenclature

$\vec{E}$	Electric field
V	Discharge electric potential
q	Charge
$\rho_{\pm}$	Charge density
$\vec{J}$	Electric current density
S	Distance between electrodes
A	Effective area of electrode tip
ε_0	Permittivity of free space
μ	Mobility of charge
R_i	Ion recombination rate
ρ	Air density
U	Flow velocity
d	Distance from electrode tip to hotwire
I_{hw}	Heat current for hotwire
R_{hw}	Hotwire resistance
α	Temperature coefficient of the resistance
A_{hw}	Surface area of hotwire
V_{hw}	Output voltage on hotwire

ent for electro-conjugate fluid [14]. For air pumping, the result of the momentum transfer is a bulk air movement commonly called the ion wind, and it has recently attracted more interest as it features several advantages: low weight, simplicity, robustness, lack of moving parts, and low power consumption. As a result, ionic air pumping has been applied in airflow control applications [15], cooling applications [16], propulsion technology [17], micro-pump design [11], gas spectrometry [18], noise control [19], precipitation filtering [20–22], bio-electronic device [23–25], synthetic jet [26]. Integration of EHD force to ionic pumping has also been used for spectrometry [27], vibrating element [28] or aerosol sampling [29,30].

Many authors have reported the characteristics of various electrode arrangements, which are typically point-to-plane [31], point-to-grid [32], point-to-ring [33] or wire-to-plate [34]. Other modifications, including wire-to-inclined wing [16], parallel plates [35], wire-to-rod [36], rod-to-plate [37], point-to-parallel plate [38], wire-to-cylinder [39], sphere-to-sphere [37], wire-to-wire [40], point-to-wire [32], point-to-cylinder [41], and conical electrode [42] have been recently suggested. The fundamental requirements of the above systems are a high-curvature electrode that generates ions and a low-curvature reference electrode, which is placed downstream to define the movement of the charged particles. Ion wind is generated at high-curvature locations, yielding high velocity near the surface of the reference electrode. The citations above provide great references in the field although actual designs of a ready-to-use device were not always provided.

Depending on the prospective application, one may find that charge from ionic wind needs to be neutralized or controllably minimized. Owing to the charge, ion wind on one hand brings unique applications in flow directed to targets, but on the other hand raises significant challenges in designing a millimetre-scale device because the charge tends to attach to the wall, therefore most of the works for ionic air pumping are with rather large systems where a far-field boundary condition is applied [43]. Although in some cases the accumulated space charge was used as the sensing source for very low velocimetry [23], in general the discharge ion current and the space charge need to be compensated for by electrons in the downstream space to prevent charging of the device [44,45]. Other problems also exist, such as the application in inertial sensing, where the flow must be able to freely vibrate in three dimensional space under inertial force, which is however dominated by electrostatic force in limited space [46–49]. In bio-applications, the aerosol particles with highly reactive ionization products are destructive for living cells, spore or viruses [50,51], therefore neutralization with gaseous counter-ions or corona neutralizer is also attractive for the formation of zero-charged aerosol [52]. One of the proposals has been the mixing of positively and negatively charged particles produced by electrohydrodynamics atomization from several independent spray sources [53,54]. Another application of neutralized, or mildly neutralized, ion wind is for electrospun polymer nanofiber to overcome the intrinsic instability of the process [55].

In this paper, we present an ion wind pumping device with a unique bipolar discharge configuration using electrodes arranged symmetrically from a single power source, thus minimizing the footprint. The experiment and simulation show that with such a symmetrical configuration, the air movement can be optimized to be parallel to the axes of the electrodes, and directed away from the device. It is well-known that ion wind can adjust its flow rate by alternating the discharging voltage/current with utilizing an external flow meter as a calibration tool, thus we propose a feasible approach by integrating a “ready-used” calibrating element into device as a hotwire anemometer, which has been widely used in inertial fluidic sensors [56,57]. With both charges simultaneously released from a power source, the amount of net charge released out of the device is small and in principle can be controlled in various ways, for example by alternating the mixing condition [52]. Owing to the easy scalability of the configuration and the low net charge, the proposed system is beneficial for applications with space constraints [58], and for applications where a neutralized ion wind is required, such as fluidic amplifiers, fluidic oscillators or fluidic actuators [59–61]. This gives the device a hybrid application of micro pump for outer space use and micro discharge for internal use. This study is also promising for vortex or convective inertial devices [62,63], particle separation and extraction into portable microfluidic labs-on-a-chip [64]. Other prospective views of this configuration are towards the microfluidics-to-mass spectrometry to provide coupling, mixing methods between microfluidic devices and mass spectrometers [65–67], pharmaceutical inhalation aerosol by bipolarly charged particles [68] or to generate mildly charged particles for insecticide dispensing where one electrode sprays the formulation of interest [69].

In the remaining part of the paper, the design and working principle of the device are described, followed by experimental and numerical setup. The air flow is validated by the integrated thermal sensing elements (hotwires) implemented at several positions along the downstream channel. The simulation is conducted in an open-source code environment, OpenFOAM. The device itself is easy-to-build and can be implemented cost effectively because of its simple and commercially available components.

2. Working principle

An ion wind generator can be realized with various designs, a typical needle-to-ring configuration consisting of a corona electrode as a pin and a collector electrode as a ring is shown in Fig. 1a. Ion wind is generated at the pin and yields high velocity near the surface of the counter electrodes, where the charge is neutralized. In our configuration, two electrodes of opposite polarity are placed in parallel, and generate charged particles from a single power source (Fig. 1b). This is principally different from multi actuator designs powered from different power sources, providing not only cost savings due to single power source, but also enabling a charge-balanced design with simultaneous charge neutralization as explained below. In our design, both electrodes serve as emitters, and also represent the reference electrode defining the electric field.

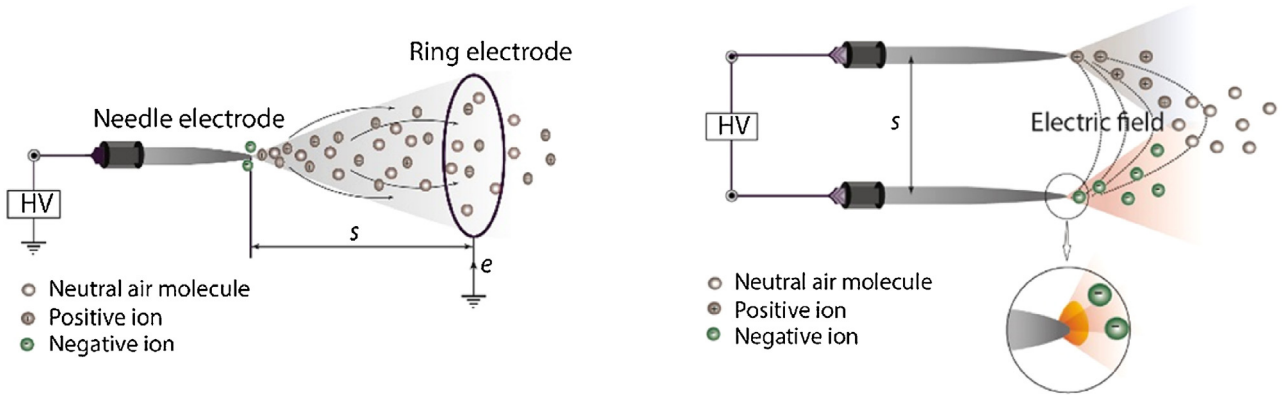

Fig. 1. Schematic view of design. Left is typical point-to-ring configuration, right is our proposed bipolar configuration.

The ion wind is simultaneously generated by both pins. The charge moves with the electric field and the resulting drift, which in turn redistributes itself across the space. The pin tip can be modelled as a protruding hemisphere with extremely high curvature attached to the pin body, which focuses the electric field outwards and nearly parallel to the pin axis. Thus, after being generated at the vicinity of tips, ion clouds (charged particles) gain an initial momentum to move in the direction away from the pin tips and in parallel with the electrodes (inset in Fig. 1b). Under the impact of the electric field between two electrodes, the clouds of oppositely charged ions from two electrodes tend to impinge on each other at the middle of electrode interspace, preventing them from reaching the counter electrodes. Due to high speed of ion wind and its forwarding momentum, the bulk of ions moves forward, resulting in net flow.

A single direct current high-voltage generator is connected to the pins. The generator is isolated and powered by a battery. The isolation ensures that the current measured at the negative polarity and representing the creation of the negative charge, is the mirror image of the current at the positive polarity for the positive charge.

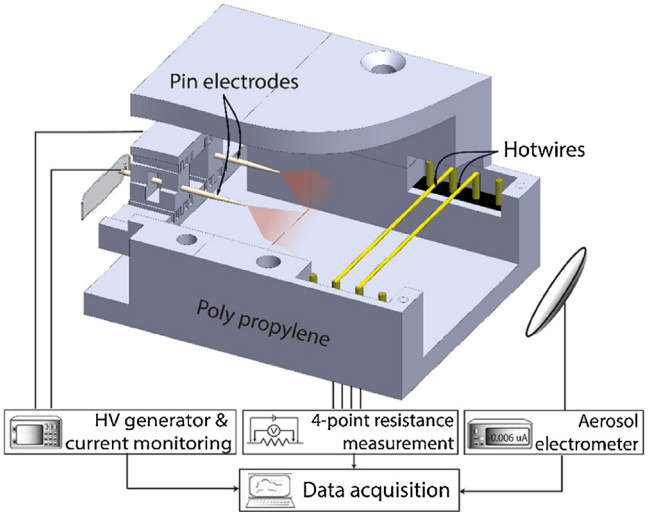

Fig. 2. Schematic design of device and measurement setup. A battery operated high voltage generator is connected to parallel pin electrodes and the ion wind is measured by hotwires heated by constant current.

3. Design and experimental setup

In order to show the flow generation capability of the device, we designed and fabricated a transparent prototype made by polypropylene with a mechanical precision of 20 μm as shown in Fig. 2. The internal cross section is 15 mm height × 20 mm width. The pin electrodes are held, aligned and positioned at one end of the device. All parts are designed for mechanical assembly via press fitting and a small amount of conformal coating is applied at the electrode holder to ensure electric isolation.

The electrodes are stainless steel SUS304, each 8 mm long and 0.4 mm in diameter, and placed in parallel with each other. The spherical radius of the pin tip is approximately 80 μm. The distance between the pins is adjustable with experiments carried out at 5 mm, 7 mm and 9 mm separation.

For the electronics part, a high voltage generator (Kyoshin Denki Ltd.), battery operated, capable of generating 10 kV direct current is connected to the pins. The discharge current is recorded at the negative electrode by a precision measuring circuit, which is integrated in the high voltage generator. The system is calibrated with high voltage generator and high voltage meter (Japan Finechem Ltd.). The isolation between the electrodes is guaranteed by two polypropylene (PP) blocks with leak current <10 nA measured between the electrode contact points. Because of the isolation from external sources, the current at both electrodes is equal in size as dictated by Kirchhoff's current law.

The ion wind generated in the device is measured by an array of 8 hotwires placed across the downstream channel starting from a distance of 12.5 mm downstream and is aligned in the plane of the electrodes. The spacing between the hotwires is 2.5 mm thus the hotwire array in total monitors a range of 17.5 mm streamwise. The hotwire, made of gold, is bonded to the electric stands embedded in the device's body for signal reading. The hotwire has a diameter of 25 μm and length of 24 mm, and its temperature coefficient of resistance is measured as 3700 ppm/°C.

By comparing the discharge I–V characteristics with and without the existence of hotwires, the minimum distance of 12.5 mm was confirmed to not have any influence on the discharge itself. The measurement of I–V characteristic of the device is repeated 8 times, corresponding to each velocity monitoring at each hotwire. The hotwires are alternatively turned on to prevent the cross effect of heat transfer between them. The hotwire is heated by constant current of 0.2 A and its voltage is read out by a digital multimeter. Data is streamed to the computer using a LabVIEW DAQ6220 data acquisition system with a sampling rate of 1 Hz. Conversion from the hotwire voltage to average air velocity is calculated by a self-developed C-code routine.

In addition, the net charge of the released ion wind is measured using an aerosol electrometer 3068 (TSI). The results were also recorded at 1 Hz and averaged over every 60 s. All the mea-

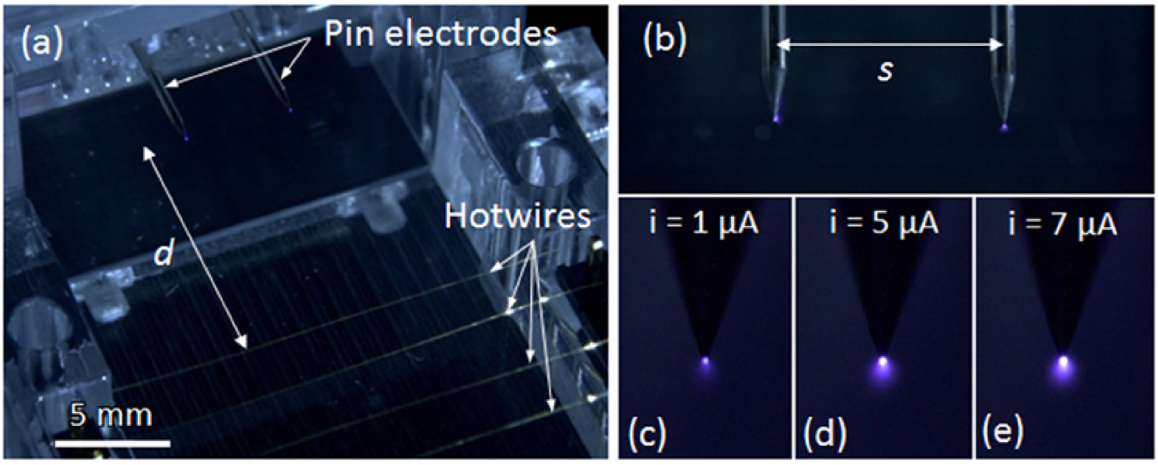

Fig. 3. (a) Fabricated device showing pin electrodes and hotwires, (b) the bipolar corona simultaneously seen at both pin tips, (c)–(e) corona glows at different discharge currents.

surements were carried out at 24 °C and 55% relative humidity at atmospheric pressure.

Fig. 3 shows pictures of the prototype in operation, where the bipolar corona discharge is observable at both pin electrodes. The observed corona glows reveal that the pin tips are similar to a sphere partly embedded into the pin body and only a small partition at the top hemisphere is unembedded and thus has extremely high curvature, which focuses the electric field outwards and almost parallel to the pin axis.

4. Numerical modeling of the device

Many numerical analyses have been carried out to understand the EHD flow in different discharge configurations. Those studies solved mass and momentum conservation equations (flow field) coupled with the Poisson and charge conservation equations (electric and charge fields). For the unipolar corona discharge mode, various EHD flow simulations for different electrode geometries were carried out for the steady-state flow [17,70,71]. On the other hand, sophisticated bipolar simulations were performed for the glow discharge [72], aerodynamic flow control [73] and a review of numerical studies of EHDs can be seen in the work of Adamiak [74]. In this part, to avoid the complications of modeling of the discharge itself, we deploy multi physics simulation to analyse the flow characteristics of our system by treating the corona as a boundary condition.

The electric field $\vec{E}$ is represented as the gradient of an electric potential V, $\vec{E} = -\nabla V$ calculated by Gauss' law and is written by the Poisson equation:

$$\nabla.\vec{E} = -\nabla^2 V = q/\varepsilon_0 \tag{1}$$

where ε_0 is the permittivity of free space and $q = q_+ - q_-$ is the total charge of from the positive and negative pins.

The charge drift creates a total electric current density $\vec{J}$, without considering the external bulk flow and neglecting the ion diffusion, the total electric current density is the sum of the positive and negative current density $\vec{J} = \rightarrow J_+ + \rightarrow J_- = \pm\mu q_\pm \vec{E} + q_\pm \vec{U}$ (where μ is mobility of charge). Because the total charge is conserved, the total current density has a zero divergence $\nabla.\vec{J} = 0$. The continuity of the positive/negative current density is described by the ion recombination, which is $R_i q_+ q_- / q_e$ (where R_i and q_e are ion recombination rate and electron charge).

$$\rightarrow J_\pm = \pm\mu q_\pm \vec{E} + q_\pm \vec{U} \tag{2-1}$$

$$\nabla.\rightarrow J_\pm = \mp R_i q_+ q_- / q_e \tag{2-2}$$

$$\nabla.(\rightarrow J_+ + \rightarrow J_-) = 0 \tag{2-3}$$

For the fluidic aspect, the flow is assumed to be incompressible Newtonian fluid and is considered at steady state. The buoyancy force due to temperature variations is neglected. The flow is then described by the Navier–Stokes equations, including conservations of momentum and of mass density. The impact of the electric field

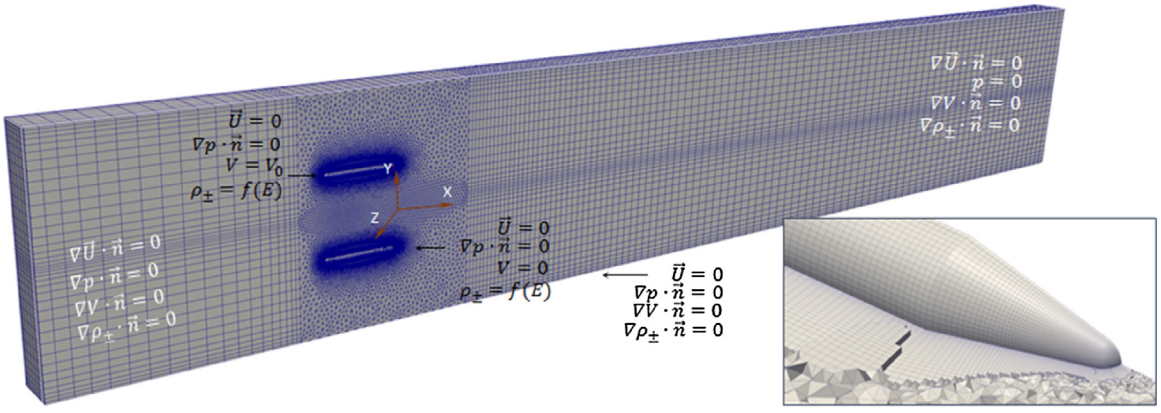

Fig. 4. Meshing and boundary conditions for numerical setup of device. The inset shows the meshing at electrode tip vicinity.

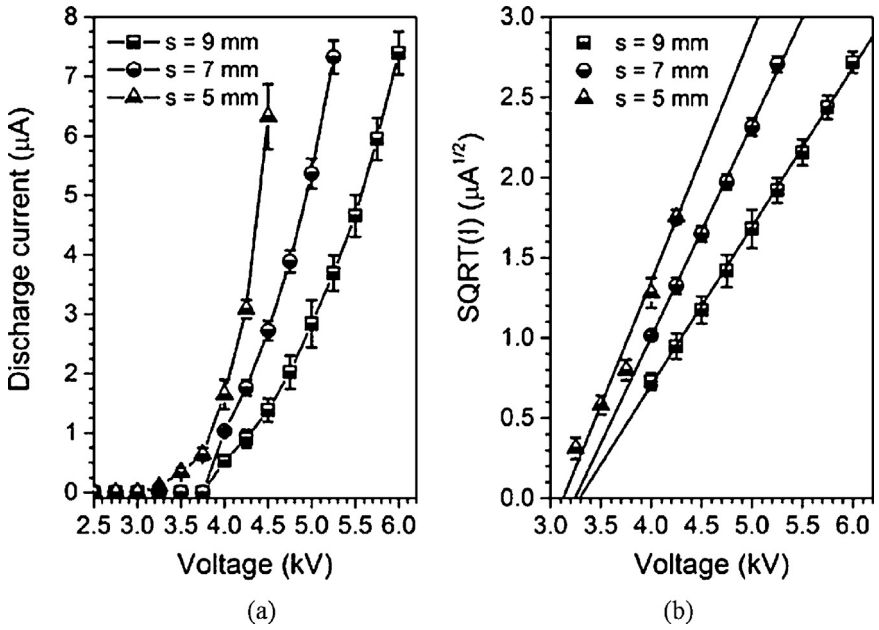

Fig. 5. (a) I–V of bipolar configuration for electrode span = 5, 7, 9 mm and (b) relation of $\sqrt{I} - V$ (b). The error bar is standard deviation from 8 repeats.

to the momentum of the gas is described by the volume force $q\vec{E}$ on the right-hand side of Eq. (3),

$$\nabla.\left(\vec{U}\vec{U}\right) - \vartheta\nabla.\left(\nabla\vec{U}\right) = -\nabla p + q\vec{E}/\rho \quad (3)$$

$$\nabla.\vec{U} = 0 \quad (4)$$

The solutions of Eqs. (1)–(4) are obtained by the development of a solver in the finite volume library OpenFOAM [75]. For a typical corona discharge, the electric field magnitude $\vec{E}$ is of the order of $10^6\,\mathrm{V\,m^{-1}}$ which yields the drift velocity $\mu\vec{E} \approx 100\,\mathrm{m\,s^{-1}}$. This is much larger than the air velocity $\vec{U}$, which is of the order of several $\mathrm{m\,s^{-1}}$. Therefore, the term $q_+\vec{U}$ in Eq. (2-1) is neglected. For stable simulation, an additional solver was developed to solve Eqs. (1) and (2) only to provide the initial electric field condition for the coupled Eqs. (1)–(4) in the main solver.

The simulation domain was modelled as shown in Fig. 4. The non-slip, no-penetration fluidic condition was set on the wall of the pin electrode and the free condition was used for the other

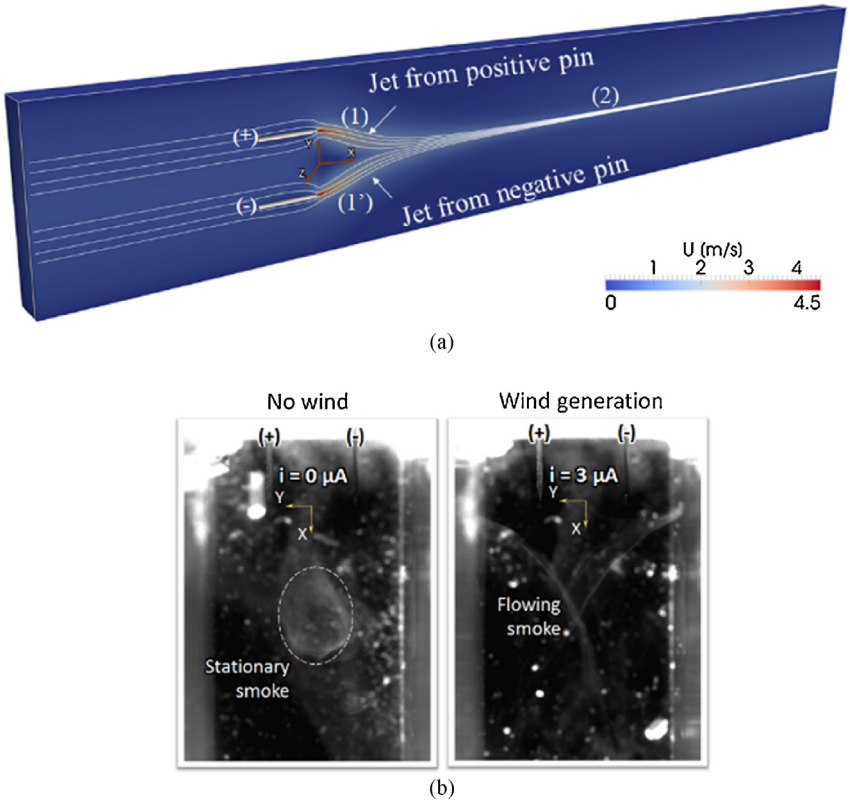

Fig. 6. (a) Simulated flow stream line and (b) flow pattern visualized by smoke.

boundaries. For the electric field, voltage was applied to the boundary of the electrodes and the Neumann condition was applied at the edges of the domain. At the electrode, we assumed that the corona discharge maintained a constant ion density $\rho_{\pm}$

$$\rho_{\pm} = I/(\mu E_w A) \quad (5)$$

where A is the total area of the tip. The electric field at the wall tip E_w is determined based on Peek's law for the barbed wire with spheroidal tip for air at standard condition, without correction for surface roughness and pressure dependency as [76]:

$$E_w = 27.2\left(\mathrm{kV/cm}\right)\left(1 + 0.54/R^{1/2}\right) \quad (6)$$

where R is the radius of the tips in units of meters. Alternatively, for the case of an arbitrary shape with double curvature, the formula differs only by a factor of 1/2 to the radius of curvature $E_w = 31\left(\mathrm{kV/cm}\right)\left[1 + 0.308/(0.5\mathrm{R})^{1/2}\right]$ [77]. By applying both equations for our configuration, we can conclude that the threshold difference is small, around 5%. Finally, with air used as the media, the following constants close the modeling portion: $\varepsilon_0 = 8.854 \times 10^{-12}\,\mathrm{C V^{-1} m^{-1}}$, $R_i = 10^{-13}\,\mathrm{m^3 s^{-1}}$, $q_e = 1.62 \times 10^{-19}\mathrm{C}$, $\mu = 1.6 \times 10^{-4}\mathrm{m^2 V^{-1} s^{-1}}$, $\rho = 1.2041\ \mathrm{kg\ m^{-3}}$ and $\nu = 15.7 \times 10^{-3}\,\mathrm{m^2}$.

5. Results and discussion

5.1. I–V characteristics

Fig. 5a shows the I–V characteristics of the system. In unipolar corona discharge, the relationship $I/V \propto V$ (Townsend relationship) is typically used in the analysis of various configurations including point-to-plane [78], point-to-grid [79] or point-to-ring [80]. We found that the I–V in our configuration better matches with the relationship $\sqrt{I} \propto V$ as shown in Fig. 5b. The match is especially accurate for electrode spans 7 mm and 9 mm, and is less followed with 5 mm. Although this relation is much less common in comparison with the Townsend relationship, this is however in agreement with the reported literature for some restricted tests, for example in point-to-plane for the positive corona with electrode distance 50 mm [81] or spherically symmetric unipolar corona [82]. In this work, the relationship $\sqrt{I} \propto V$ is used to analyse the present configuration in the next sections.

5.2. Flow pattern and net charge of ion wind

Fig. 6a presents the simulated result of the flow field. In order to facilitate the discussion, a Cartesian coordinate system is designated with the origin located at the centre of electrode interspace as shown in Fig. 6a. After being generated in the vicinity of the tips, the ion clouds gain an initial momentum to move in the direction away from the pin tips and in parallel with the electrodes. Under the interaction with the electric field between the two electrodes, the jets of oppositely charged ions tend to impinge on each other at the middle of the electrode interspace, resulting in pressure drop and charge neutralization. This causes the bulk flow of ions to move forward. The overall view of the generated ion wind demonstrates that the jet flow is maintained downstream far away from the pins. Fig. 6b shows the visualization of ion wind by smoke particles introduced to the device from both sides of pins. Without applied voltage, the smoke remains almost stationary, slowly diffusing inside the device (Fig. 6b, left). When the device is in operation and ion wind is generated, the two jet flows are demonstrated by smoke movement as shown in Fig. 6b (right).

It was confirmed that as a result of the mixing of opposite charges, the total charge of the ion wind outside the wind collector was very low. It was typically around

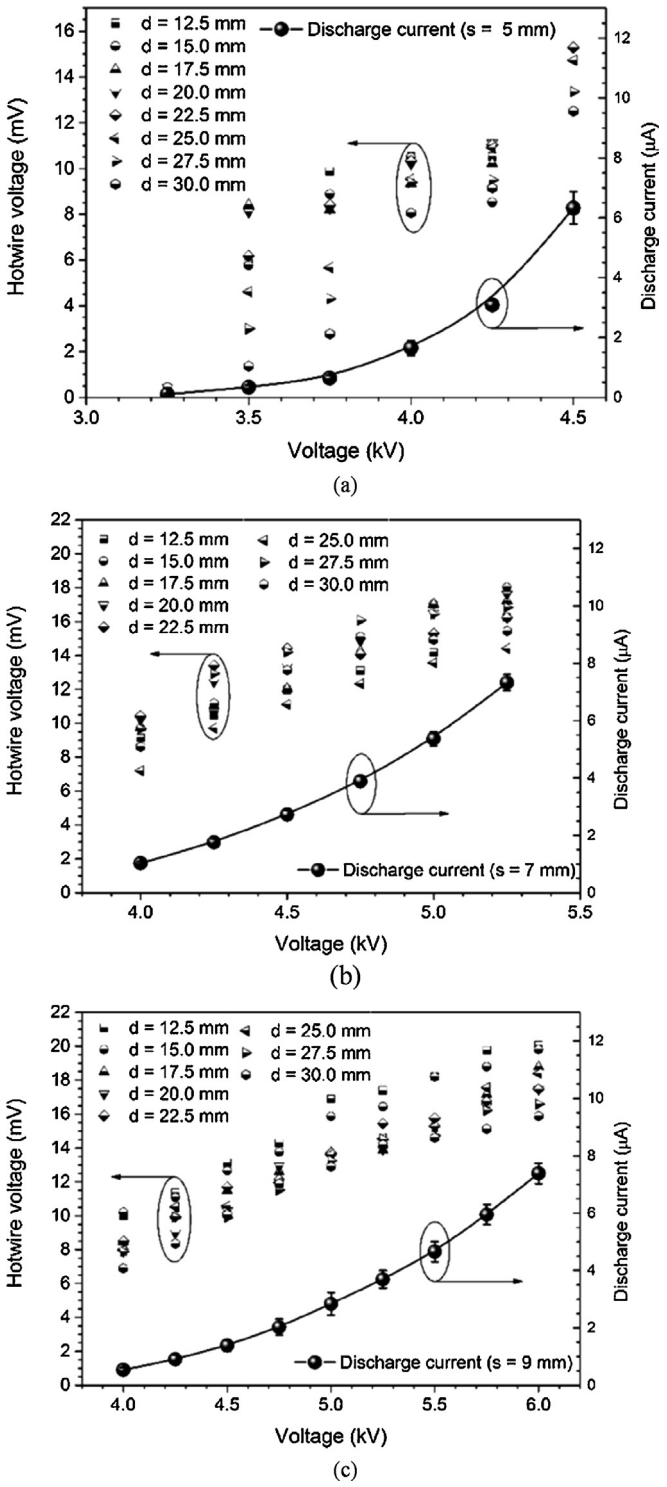

Fig. 7. Velocity measured by hotwire with electrode span of (a) 5 mm, (b) 7 mm, and (c) 9 mm.

−10 fA to +30 fA on the aerosol electrometer measured at outlet of device. This charge was almost independent of the electrode separation in experiments and is comparable with the value of the background noise, which was measured with the device turned off. Since this net charge of ion wind is very small compared with the discharge current (of the order of μA, which is 9 orders larger), this confirms that the positive and negative charges are well balanced.

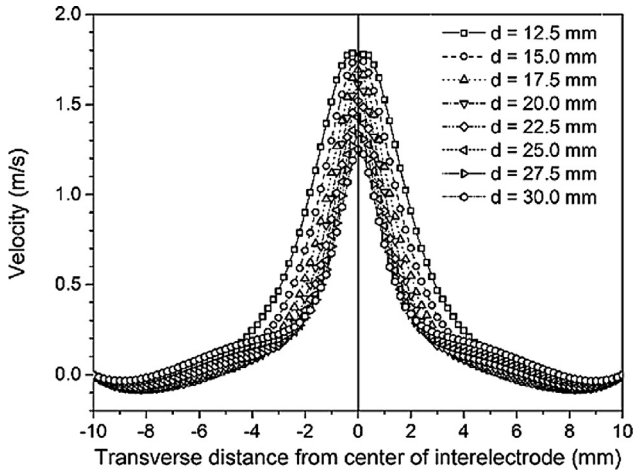

Fig. 8. Velocity profile at hotwire position, electrode distance 7 mm, discharge current 5.37 μA.

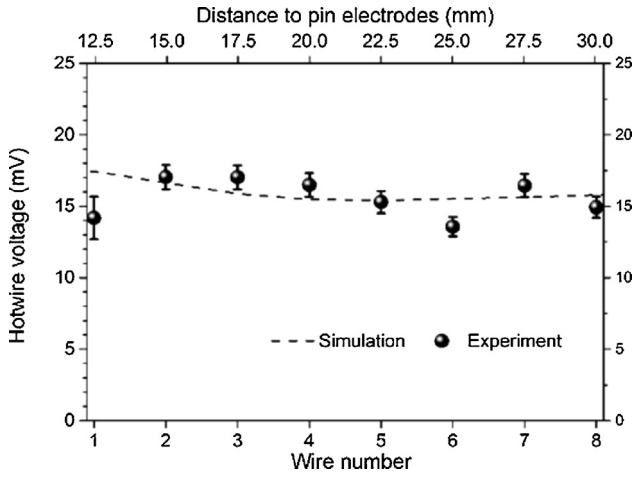

Fig. 9. Comparison of simulation and experiment. Electrode distance 7 mm, discharge current 5.37 μA, hotwire current 0.2 A.

5.3. Flow measurement by hotwire

The effect of ion wind on the temperature of the hotwire T_{hw}, heated by the current I_{hw} is determined from the equilibrium equation of heat transfer at steady state between the hotwire and air

$$I_{hw}^2 R_{hw} = hA_{hw}(T_{hw} - T_a) \tag{7}$$

where A_{hw}, h, and T_a are surface area of the hotwire, heat transfer coefficient, and ambient temperature, respectively. R_{hw} is the hotwire resistance expressed as

$$R_{hw} = R_a[1 + \alpha(T_{hw} - T_a)] \tag{8}$$

with R_a and α are the resistance at temperature T_a and the temperature coefficient of the resistance of the hotwire material, respectively.

Without corona discharge, stationary air defines the initial state of measurement by natural convection. When the corona is activated, the ion wind cools the hotwire down by forced convection. The heat transfer coefficient of forced convection [83] and natural convection [84] are respectively calculated as presented in Eqs. (9) and (10)

$$h = 0.24 + 0.56Re^{0.45}\frac{\lambda}{D} \tag{9}$$

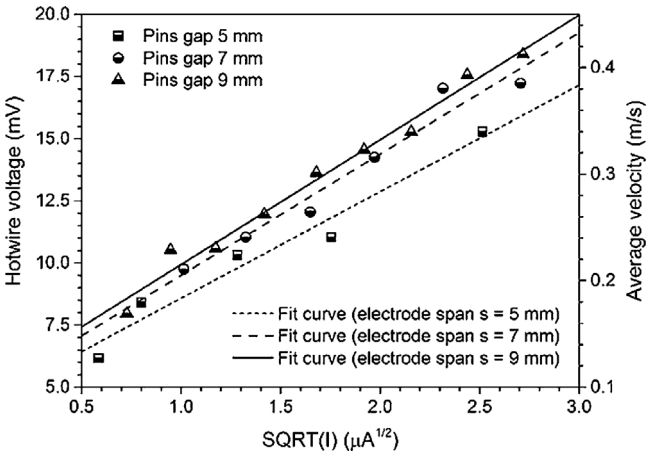

Fig. 10. Relation between hotwire output voltage and discharge current. The right axis shows the average velocity calculated from hotwire voltage.

$$h = 1.02Ra^{0.1}\frac{\lambda}{D} \tag{10}$$

where Ra is the Rayleigh number, D is the effective diameter of the hotwire, and $Re = UD\rho/\mu$ is the Reynolds number. The output voltage on the hotwire, offset to the initial value measured with still air, is measured as $V_{hw} = I_{hw}\Delta R_{hw} = I_{hw}\alpha\Delta T$. This voltage V_{hw} is shown in Fig. 7.

Electrode span of s = 5 mm creates lower velocity than the others and the flow is more unstable (see Fig. 7a). This is because as the pin separation decreases, the electrode itself becomes significant compared with the interelectrode space. Intuitively when the electrode span becomes comparable with the electrode radial dimension, the flow component towards the counter electrode increases, and the attack angle formed by two jet flows becomes larger. In other words, the flow velocity component towards the counter electrode becomes stronger. This results in a more direct collision of jet flows from the pins, introducing turbulence and reducing the streamwise flow velocity.

The above explanation is confirmed again with results in Fig. 7b and c where the electrode span is 7 mm and 9 mm, respectively. The measurement is more repeatable between different hotwires. Hotwires placed further away from the electrodes have smaller output voltage, which reflects the decay of the jet flow. The flow velocity is slightly larger with increasing electrode separation, however there is not much difference between 7 mm and 9 mm. The flow velocity profile, which cannot be revealed by hotwire anemometry, is demonstrated from simulation.

The profiles of the velocity along streamwise direction at eight hotwire locations are plotted in Fig. 8 for electrode span of 7 mm, discharge current I = 5.37 μA and discharge voltage V = 5 kV. From Fig. 8, it is evident that the peaks of the profiles decrease with increasing streamwise distance from the pin tips. This confirms that the jet decays with increasing distance from its source, as expected. The tails of these profiles have negative values, which show that there is a circulatory flow in the channel. A flow peak velocity up to 1.8 m s^{-1} is achieved. The figure implies that the device can create bulk flow movement with typical jet flow characteristics. This characteristic of the device allows us to further develop multi axis inertial units, or multi direction synthetic jets in the future.

Fig. 9 compares the hotwire anemometry result elicited in the experiment and the above simulation. The abscissa is the hotwire position and the vertical axis is the output voltage in millivolts. For direct comparison, the simulation values are expressed in terms of hotwire voltage. As it can be seen, the simulation agrees well with experiment. It is noted that because the hotwire is placed across the entire width of the device, its measurement represents the cooling

effect of the average flow velocity in hotwire plane, thus although the peak velocity decays rapidly with distance, the average velocity across the device and thus the output voltage on the hotwire decays much slower.

It is also important to note that while ion is discharged with current of several μAs, the current supplied to hotwire is six orders larger, so the effect of discharge current to the hotwire voltage is very small. In addition, because both charges are released, this error is further minimized and is negligible, therefore the voltage on hotwire can be calculated by only considering the cooling effect of the flow. This is further confirmed by turning on the corona discharge without heating the hotwire, when we observed zero output voltage.

However there was still a difference with the experimental results, particularly at the wire closest to the pin. Because the experimental device was fabricated with limited resolution, the device wall surface was unsmooth at a submillimeter scale and it was excluded from the simulation. Also the pin holder, which indeed has considerable size compared with the chamber although its location at upstream would scale down its impact, is ignored in the simulation. Finally the tolerance in pin alignment made the tolerance at the closest hotwire larger compared with the others. Better agreement can be expected if a microfabrication process is involved.

Fig. 10 presents the relationship between the output voltage on the hotwire, which is proportional to the average flow velocity, and the discharge current. The result shows that the output voltage has a linear relation with the square root of discharge current $V_{hw} \propto \sqrt{I}$. Because the relation of the flow velocity and discharge current can be estimated by the balance of kinetic energy of moving flow with discharge power, thus can be represented by hotwire anemometry in our device. It can be noted that, in the experiment, the relation $V_{hw} \propto \sqrt{I}$ also holds for all electrode spans. The power for corona discharge itself is small, for example around 25 mW and the power consumption of our electric circuit is less than 70 mW for the experimental condition in Fig. 9.

6. Conclusion

We have presented the design of a bipolar corona-based airflow generator and examined its characteristics by numerical simulations and experimental validation. The modified airflow generator is based on the simultaneous generation of both positive and negative ions using two sharp electrodes placed in parallel. The resulting neutralized ion wind is created with low power consumption. The model showed good agreement with experimental data in terms of the dynamic response. Based on the measured current–voltage curves of bipolar corona discharge, simulations of flow rate and charge distribution were carried out. The measured result of the present device has slight discrepancy with experimental data particularly at close vicinity around the electrodes. We believe that this mismatch can be improved with better fabrication process and more precise simulation of boundary conditions. The ion diffusion was not taken into account and the positive and negative coronas and their induced ions were treated equally, which is different from reality. In this regard many improvements are in progress, such as more precise simulation of the electron-ion interaction plane.

Although in theory the system is expected to have increased efficiency as the distance between the electrodes is reduced, this is limited by the geometrical constraints of the system setup. The pins and electrical connections still have finite size, impeding the airflow around the pins. It is believed that with a revised system setup, such as usage of pins with smaller diameters or utilization of a microfabrication process, the efficiency could further increase and ion wind generation of similar magnitude could be expected at lower voltage levels and reduced applied power. In addition, as for any corona-based device, external factors such as temperature, humidity and atmospheric pressure will also affect the device and need to be considered to ensure reliable operation. These improvements are currently in progress and will be reported in future publications.

References

[1] L.Y. Yeo, H.-C. Chang, P.P.Y. Chan, J.R. Friend, Microfluidic devices for bioapplications, Small 7 (2011) 12–48, http://dx.doi.org/10.1002/smll.201000946.

[2] D.J. Laser, J.G. Santiago, A review of micropumps, J. Micromech. Microeng. 14 (2004) R35–R64, http://dx.doi.org/10.1088/0960-1317/14/6/R01.

[3] L. Chen, Fabrication and characterization of a multi-stage electroosmotic pump for liquid delivery, Sens. Actuators B Chem. 104 (2005) 117–123, http://dx.doi.org/10.1016/j.snb.2004.05.013.

[4] S. Yokota, A review on micropumps from the viewpoint of volumetric power density, Mech. Eng. Rev. 1 (2014), http://dx.doi.org/10.1299/mer.2014dsm0014, DSM0014–DSM0014.

[5] V.T. Dau, T.X. Dinh, T. Katsuhiko, S. Susumu, A cross-junction channel valveless-micropump with PZT actuation, Microsyst. Technol. 15 (2009) 1039–1044, http://dx.doi.org/10.1007/s00542-009-0878-2.

[6] C.G.J. Schabmueller, M. Koch, M.E. Mokhtari, A.G.R. Evans, A. Brunnschweiler, H. Sehr, Self-aligning gas/liquid micropump, J. Micromech. Microeng. 12 (2002) 420–424, http://dx.doi.org/10.1088/0960-1317/12/4/313.

[7] K. Tanaka, V.T. Dau, R. Sakamoto, T.X. Dinh, D.V. Dao, S. Sugiyama, Fabrication and basic characterization of a piezoelectric valveless micro jet pump, Jpn. J. Appl. Phys. 47 (2008) 8615–8618, http://dx.doi.org/10.1143/JJAP.47.8615.

[8] D. Jang, K. Lee, Flow characteristics of dual piezoelectric cooling jets for cooling applications in ultra-slim electronics, Int. J. Heat Mass Transf. 79 (2014) 201–211, http://dx.doi.org/10.1016/j.ijheatmasstransfer.2014.08.013.

[9] V.T. Dau, T.X. Dinh, T.T. Bui, Jet flow generation in a circulatory miniaturized system, Sens. Actuators B Chem. 223 (2015) 820–826, http://dx.doi.org/10.1016/j.snb.2015.09.151.

[10] V.T. Dau, T.X. Dinh, Numerical study and experimental validation of a valveless piezoelectric air blower for fluidic applications, Sens. Actuators B Chem. 221 (2015) 1077–1083, http://dx.doi.org/10.1016/j.snb.2015.07.041.

[11] O.M. Stuetzer, Ion drag pumps, J. Appl. Phys. 31 (1960) 136–146, http://dx.doi.org/10.1063/1.1735388.

[12] V.V. Gogosov, G.A. Shaposhnikova, I.D. Shikhmurzaev, Qualitative analysis of electro-hydrodynamic characteristics of weakly conducting fluids, J. Appl. Math. Mech. 46 (1982) 339–346, http://dx.doi.org/10.1016/0021-8928(82)90109-5.

[13] Y. Otsubo, K. Edamura, Dielectric fluid motors, Appl. Phys. Lett. 71 (1997) 318–320, http://dx.doi.org/10.1063/1.119560.

[14] R.V. Raghavan, J. Qin, L.Y. Yeo, J.R. Friend, K. Takemura, S. Yokota, et al., Electrokinetic actuation of low conductivity dielectric liquids, Sensors Actuators B Chem. 140 (2009) 287–294, http://dx.doi.org/10.1016/j.snb.2009.04.036.

[15] T.C. Corke, C.L. Enloe, S.P. Wilkinson, Dielectric barrier discharge plasma actuators for flow control, Annu. Rev. Fluid Mech. 42 (2010) 505–529, http://dx.doi.org/10.1146/annurev-fluid-121108-145550.

[16] A. Rashkovan, E. Sher, H. Kalman, Experimental optimization of an electric blower by corona wind, Appl. Therm. Eng. 22 (2002) 1587–1599, http://dx.doi.org/10.1016/S1359-4311(02)00082-0.

[17] C. Kim, K.C. Noh, S.Y. Kim, J. Hwang, Electric propulsion using an alternating positive/negative corona discharge configuration composed of wire emitters and wire collector arrays in air, Appl. Phys. Lett. 99 (2011) 2013–2016, http://dx.doi.org/10.1063/1.3636409.

[18] D.I. Carroll, I. Dzidic, R.N. Stillwell, K.D. Haegele, E.C. Horning, Atmospheric pressure ionization mass spectrometry. Corona discharge ion source for use in a liquid chromatograph–mass spectrometer-computer analytical system, Anal. Chem. 47 (1975) 2369–2373, http://dx.doi.org/10.1021/ac60364a031.

[19] A. Das Gupta, S. Roy, Noise control of subsonic cavity flows using plasma actuated receptive channels, J. Phys. D Appl. Phys. 47 (2014) 502002, http://dx.doi.org/10.1088/0022-3727/47/50/502002.

[20] M. Meziane, O. Eichwald, J.P. Sarrette, O. Ducasse, M. Yousfi, F. Marchal, Electro-hydrodynamics and kinetic modelling of polluted air flow activated by multi-tip-to-plane corona discharge, J. Appl. Phys. 113 (2013) 153302, http://dx.doi.org/10.1063/1.4801879.

[21] B. Chua, A.S. Wexler, N.C. Tien, D.A. Niemeier, B.A. Holm, Collection of liquid phase particles by microfabricated electrostatic precipitator, J. Microelectromech. Syst. 22 (2013) 1010–1019.

[22] A.S. Chua, N.C. Tien, D.A. Niemeier, B.A. Holmén, Micro corona based particle steering air filter, Sens. Actuators A Phys. 196 (2013) 8–15, http://dx.doi.org/10.1016/j.sna.2013.03.029.

[23] B. Chua, J.J. Pak, Miniaturized corona flow sensor operating in drift mobility increment mode for low flow velocity measurement, Sens. Actuators A Phys. 224 (2015) 65–71, http://dx.doi.org/10.1016/j.sna.2015.01.022.

[24] A.K. Sen, J. Darabi, D.R. Knapp, Design, fabrication and test of a microfluidic nebulizer chip for desorption electrospray ionization mass spectrometry, Sens. Actuators B Chem. 137 (2009) 789–796, http://dx.doi.org/10.1016/j.snb.2009.02.002.

[25] V.T. Dau, T.T. Bui, T.X. Dinh, T. Terebessy, H.T. Phan, Absolute pressure sensing with bipolar corona discharge: design, simulation and experimental validation, 29th IEEE Int. Conf. Micro. Electro. Mech. Syst. (2016) 820–823.
[26] A. Belinger, N. Naudé, J.P. Cambronne, D. Caruana, Plasma synthetic jet actuator: electrical and optical analysis of the discharge, J. Phys. D Appl. Phys. 47 (2014) 345202, http://dx.doi.org/10.1088/0022-3727/47/34/345202.
[27] S. Liu, C. Huang, C. Shen, H. Jiang, Y. Chu, A novel driving mode for ion shutter based on alternating current superposition and its application to ion mobility spectrometry, Sens. Actuators B Chem. 211 (2015) 102–110, http://dx.doi.org/10.1016/j.snb.2015.01.061.
[28] B. Chua, V.J. Logeeswaran, M. Chan, H. Park, D.A. Horsley, N.C. Tien, Wideband mechanical excitation by a microcorona-driven vibrating element, J. Microelectromech. Syst. 24 (2015) 224–231.
[29] G. Pardon, L. Ladhani, N. Sandström, M. Ettori, G. Lobov, Aerosol sampling using an electrostatic precipitator integrated with a microfluidic interface, Sensors Actuators B. Chem. 212 (2015) 344–352, http://dx.doi.org/10.1016/j.snb.2015.02.008.
[30] B. Chua, A.S. Wexler, N.C. Tien, D.A. Niemeier, B.A. Holmen, Electrical mobility separation of airborne particles using integrated microfabricated corona ionizer and separator electrodes, J. Microelectromech. Syst. 18 (2009) 4–13, http://dx.doi.org/10.1109/JMEMS.2008.2011123.
[31] B.L. Henson, Toward a fundamental model for steady point-plane corona discharges, J. Appl. Phys. 55 (1984) 150–157, http://dx.doi.org/10.1063/1.332878.
[32] I.Y. Chen, M.Z. Guo, K.S. Yang, C.C. Wang, Enhanced cooling for LED lighting using ionic wind, Int. J. Heat Mass Transf. 57 (2013) 285–291, http://dx.doi.org/10.1016/j.ijheatmasstransfer.2012.10.015.
[33] A.M. Drews, L. Cademartiri, G.M. Whitesides, K.J.M. Bishop, Electric winds driven by time oscillating corona discharges, J. Appl. Phys. 114 (2013), http://dx.doi.org/10.1063/1.4824748.
[34] D.B. Go, S.V. Garimella, T.S. Fisher, R.K. Mongia, Ionic winds for locally enhanced cooling, J. Appl. Phys. 102 (2007), http://dx.doi.org/10.1063/1.2776164.
[35] P.J. McKinney, J.H. Davidson, D.M. Leone, Current distributions for barbed plate-to-plane coronas, IEEE Trans. Ind. Appl. 28 (1992) 1424–1431, http://dx.doi.org/10.1109/28.175297.
[36] B. Komeili, J.S. Chang, G.D. Harvel, C.Y. Ching, D. Brocilo, Flow characteristics of wire-rod type electrohydrodynamic gas pump under negative corona operations, J. Electrostat. 66 (2008) 342–353, http://dx.doi.org/10.1016/j.elstat.2008.02.004.
[37] H. Toyota, S. Zama, Y. Akamine, S. Matsuoka, K. Hidaka, Gaseous electrical discharge characteristics in air and nitrogen at cryogenic temperature, IEEE Trans. Dielectr. Electr. Insul. 9 (2002) 891–898, http://dx.doi.org/10.1109/TDEI.2002.1115482.
[38] P. Zhao, S. Portugal, S. Roy, Efficient needle plasma actuators for flow control and surface cooling, Appl. Phys. Lett. 107 (2015) 033501, http://dx.doi.org/10.1063/1.4927051.
[39] B. Kim, S. Lee, Y.S. Lee, K.H. Kang, Ion wind generation and the application to cooling, J. Electrostat. 70 (2012) 438–444, http://dx.doi.org/10.1016/j.elstat.2012.06.002.
[40] J. Darabi, C. Rhodes, CFD modeling of an ion-drag micropump, Sens. Actuators A Phys. 127 (2006) 94–103, http://dx.doi.org/10.1016/j.sna.2005.10.051.
[41] L. Li, S.J. Lee, W. Kim, D. Kim, An empirical model for ionic wind generation by a needle-to-cylinder dc corona discharge, J. Electrostat. 73 (2015) 125–130, http://dx.doi.org/10.1016/j.elstat.2014.11.001.
[42] O. Fawole, M. Tabib-Azar, A novel geometry for a corona wind electrohydrodynamic pump, IEEE Sensors 2014 Proc., IEEE (2014) 452–454, http://dx.doi.org/10.1109/ICSENS.2014.6985032.
[43] M. Riherd, S. Roy, Measurements and simulations of a channel flow powered by plasma actuators, J. Appl. Phys. 112 (2012) 053303, http://dx.doi.org/10.1063/1.4749250.
[44] K. Nishiyama, H. Kuninaka, Discussion on performance history and operations of hayabusa ion engines, Trans. Japan Soc. Aeronaut. Sp. Sci. Aerosp. Technol. Japan 10 (2012) Tb_1–Tb_8, http://dx.doi.org/10.2322/tastj.10.Tb_1.
[45] D.M. Goebel, I. Katz, Fundamentals of Electric Propulsion: Ion and Hall Thrusters, John Wiley & Sons, Hoboken, New Jersey, 2008.
[46] V.T. Dau, T. Shiozawa, D.V. Dao, H. Kumagai, S. Sugiyama, A dual axis gas gyroscope utilizing low-doped silicon thermistor, 18th IEEE Int. Conf. Micro Electro Mech. Syst. 2005. MEMS 2005 (2005) 626–629, http://dx.doi.org/10.1109/MEMSYS.2005.1454007.
[47] R.B. Schlesinger, M. Lippmann, Particle deposition in the trachea: in vivo and in hollow casts, Thorax 31 (1976) 678–684, http://dx.doi.org/10.1136/thx.31.6.678.
[48] Y. Fukatsu, E. Nomura, K. Matsu, Gas rate gyro, US4941353, 1990.
[49] V.T. Dau, T. Otake, T.X. Dinh, D.V. Dao, S. Sugiyama, A multi axis fluidic inertial sensor, Proc. IEEE Sensors, IEEE (2008) 666–669, http://dx.doi.org/10.1109/ICSENS.2008.4716529.
[50] E.-H. Lee, B. Chua, A. Son, Micro corona discharge based cell lysis method suitable for inhibitor resistant bacterial sensing systems, Sens. Actuators B Chem. 216 (2015) 17–23, http://dx.doi.org/10.1016/j.snb.2015.04.030.
[51] B. Chua, A. Son, Sterilization of *Escherichia coli* O157:H7 using micro corona ionizer, Biomed. Microdevices 16 (2014) 355–363, http://dx.doi.org/10.1007/s10544-014-9838-4.
[52] V.N. Morozov, Generation of biologically active nano-aerosol by an electrospray-neutralization method, J. Aerosol Sci. 42 (2011) 341–354, http://dx.doi.org/10.1016/j.jaerosci.2011.02.008.
[53] J.C. Almekinders, C. Jones, Multiple jet electrohydrodynamic spraying and applications, J. Aerosol Sci. 30 (1999) 969–971, http://dx.doi.org/10.1016/S0021-8502(98)00755-1.
[54] D. Camelot, J.C.M. Marijnissen, B. Scarlett, Bipolar coagulation process for the production of powders, Ind. Eng. Chem. Res. 38 (1999) 631–638, http://dx.doi.org/10.1021/ie980435j.
[55] O. Salata, Tools of nanotechnology: electrospray, Curr. Nanosci. 1 (2005) 25–33, http://dx.doi.org/10.2174/1573413052953192.
[56] V.T. Dau, D. Viet Dao, S. Sugiyama, A 2-DOF convective micro accelerometer with a low thermal stress sensing element, Smart Mater. Struct. 16 (2007) 2308–2314, http://dx.doi.org/10.1088/0964-1726/16/6/034.
[57] D.V. Dao, V.T. Dau, T.X. Dinh, S. Sugiyama, A fully integrated MEMS-based convective 3-DOF gyroscope, Transducers 2007–2007 Int. Solid-State Sensors, Actuators Microsystems Conf., IEEE (2007) 1211–1214, http://dx.doi.org/10.1109/SENSOR.2007.4300354.
[58] V.T. Dau, T.T. Bui, T.X. Dinh, T. Terebessy, Pressure sensor based on bipolar discharge corona configuration, Sens. Actuators A Phys. 237 (2016) 81–90, http://dx.doi.org/10.1016/j.sna.2015.11.024.
[59] Y. Cai, Y. Zhao, Ion discharge gyroscope, US8146423, 2012.
[60] V.T. Dau, D.V. Dao, T. Shiozawa, S. Sugiyama, Simulation and fabrication of a convective gyroscope, IEEE Sens. J. 8 (2008) 1530–1538, http://dx.doi.org/10.1109/JSEN.2008.925457.
[61] T. Shiozawa, V.T. Dau, D.V. Dao, H. Kumagai, S. Sugiyama, A dual axis thermal convective silicon gyroscope, Micro-Nanomechatronics Hum. Sci. 2004 Fourth Symp. Micro-Nanomechatronics Information-Based Soc. 2004., IEEE (2004) 1–6, http://dx.doi.org/10.1109/MHS.2004.1421318.
[62] V.T. Dau, D.V. Dao, T. Shiozawa, H. Kumagai, S. Sugiyama, A single-axis thermal convective gas gyroscope, Sens. Mater. 17 (2005) 453–463.
[63] H. Chang, P. Zhou, Z. Xie, X. Gong, Y. Yang, W. Yuan, Theoretical modeling for a six-DOF vortex inertial sensor and experimental verification, J. Microelectromech. Syst. 22 (2013) 1100–1108, http://dx.doi.org/10.1109/JMEMS.2013.2271862.
[64] G.T. Roman, R.T. Kennedy, Fully integrated microfluidic separations systems for biochemical analysis, J. Chromatogr. A 1168 (2007) 170–188, http://dx.doi.org/10.1016/j.chroma.2007.06.010, Discussion 169.
[65] X. Wang, L. Yi, N. Mukhitov, A.M. Schrell, R. Dhumpa, M.G. Roper, Microfluidics-to-mass spectrometry: a review of coupling methods and applications, J. Chromatogr. A 1382 (2015) 98–116, http://dx.doi.org/10.1016/j.chroma.2014.10.039.
[66] F. Haghighi, Z. Talebpour, A. Sanati-Nezhad, Through the years with on a chip gas chromatography: a review, Lab Chip 15 (2015) 2559–2575, http://dx.doi.org/10.1039/C5LC00283D.
[67] V.T. Dau, T.X. Dinh, D.V. Dao, S. Sugiyama, Design and simulation of a novel 3-DOF MEMS convective gyroscope, IEEJ Trans. Sens. Micromach. 128 (2008) 219–224, http://dx.doi.org/10.1541/ieejsmas.128.219.
[68] W. Glover, H.-K. Chan, Electrostatic charge characterization of pharmaceutical aerosols using electrical low-pressure impaction (ELPI), J. Aerosol Sci. 35 (2004) 755–764, http://dx.doi.org/10.1016/j.jaerosci.2003.12.003.
[69] L.F. Whitmore, J.F. Hughes, N. Harrison, M. Abela, P. O'Rourke, Enhanced efficiency of electrostatically charged insecticide aerosols, Pest Manag. Sci. 57 (2001) 432–436, http://dx.doi.org/10.1002/ps.292.
[70] A.A. Martins, Simulation of a wire-cylinder-plate positive corona discharge in nitrogen gas at atmospheric pressure, Phys. Plasmas 19 (2012), http://dx.doi.org/10.1063/1.4725499.
[71] C. Kim, K.C. Noh, J. Hyun, S.G. Lee, J. Hwang, H. Hong, Microscopic energy conversion process in the ion drift region of electrohydrodynamic flow, Appl. Phys. Lett. 100 (2012), http://dx.doi.org/10.1063/1.4729443.
[72] K. Yanallah, F. Pontiga, A. Castellanos, Numerical simulation of an oxygen-fed wire-to-cylinder negative corona discharge in the glow regime, J. Phys. D Appl. Phys. 44 (2011) 055201, http://dx.doi.org/10.1088/0022-3727/44/5/055201.
[73] J.-C. Matéo-Vélez, P. Degond, F. Rogier, A. Séraudie, F. Thivet, Modelling wire-to-wire corona discharge action on aerodynamics and comparison with experiment, J. Phys. D. Appl. Phys. 41 (2008) 035205, http://dx.doi.org/10.1088/0022-3727/41/3/035205.
[74] K. Adamiak, Numerical models in simulating wire-plate electrostatic precipitators: a review, J. Electrostat. 71 (2013) 673–680, http://dx.doi.org/10.1016/j.elstat.2013.03.001.
[75] OpenFOAM® | The OpenFOAM Foundation, (n.d.). http://openfoam.org/.
[76] F.W. Peek, Dielectric Phenomena in High Voltage Engineering, McGraw-Hill, New York, 1978.
[77] M. Goldman, A. Goldman, Corona Discharges, Academic Press, Inc., 1978, http://dx.doi.org/10.1016/B978-0-12-349701-7.50009-2.
[78] M. Robinson, Movement of air in the electric wind of the corona discharge, Trans. Am. Inst. Electr. Eng. Part I Commun. Electron. 80 (1961) 143–150, http://dx.doi.org/10.1109/TCE.1961.6373091.
[79] K. Yamada, An empirical formula for negative corona discharge current in point-grid electrode geometry, J. Appl. Phys. 96 (2004) 2472–2475, http://dx.doi.org/10.1063/1.1775301.
[80] P. Giubbilini, The current-voltage characteristics of point-to-ring corona, J. Appl. Phys. 64 (1988) 3730–3732, http://dx.doi.org/10.1063/1.341368.
[81] A.F. Kip, Onset studies of positive point-to-plane corona in air at atmospheric pressure, Phys. Rev. 55 (1939) 549–556, http://dx.doi.org/10.1103/PhysRev.55.549.
[82] R.S. Sigmond, Simple approximate treatment of unipolar space-charge-dominated coronas: the Warburg law and the saturation current, J. Appl. Phys. 53 (1982) 891–898, http://dx.doi.org/10.1063/1.330557.

[83] M. Mikheyev, Fundamentals of Heat Transfer, Peace Publisher, Moscow, 1968.
[84] I. Mabuchi, T. Tanaka, Experimental study on effect of vibration on natural convective heat transfer from a horizontal fine wire, Bull. JSME 10 (1967) 808–816, http://dx.doi.org/10.1299/jsme1958.10.808.

Biographies

Van Thanh Dau received the B.S. degree in aerospace engineering from Hochiminh City University of Technology, Vietnam, in 2002, and the M.S. and Ph.D. degrees in micromechatronics from Ritsumeikan University, Japan, in 2004 and 2007, respectively. From 2007 to 2009, he was a Postdoctoral Fellow with Japan Society for the Promotion of Science (JSPS) at Micro Nano Integrated Devices Laboratory, Ritsumeikan University. Since 2010 he has been with Research Group, Sumitomo Chemical Co., Ltd. where he works on integrated micro electrospray and atomization methods. His current research subjects are micro fluidics, electro hydrodynamics, microsensors and microactuators. He is the author and co-author of more than 70 scientific articles and 19 inventions.

Thien Xuan Dinh received the B.S. degree in aerospace engineering from Hochiminh City University of Technology in 2002, Vietnam and the M.Sc. and Ph.D. degrees in mechanical engineering from Ritsumeikan University in 2004 and 2007, respectively. He was recipient of Japan Government Scholarship (MEXT) for Outstanding Student to pursuits his M. Sc. and Ph. D. courses and Japan Society for the Promotion of Science postdoctoral fellowship from 2011 to 2013. His general research interest is computation of fluid flow. The large parts of his research are turbulence modeling using Large Eddy Simulation, multiphase modeling using Volume of Fluid technique, and simulation of turbulence and dispersion. Recently, he has focused on computation of fluid flow for developing microfluidic devices as electrohydrodynamics, microsensors, micropump, and micromixer for biochemical engineering.

Tibor Terebessy received his M.S. degree with honour in plasma physics from Comenius University, Slovakia, in 1998 and his Ph.D. degree in electronics engineering from Shizuoka University, Japan, in 2002. He was then awarded a Postdoctoral Fellowship by the Japan Society for the Promotion of Science (JSPS), continuing his research in large area microwave discharges and their industrial applications at Graduate School of Electronic Science and Technology, Shizuoka University, Japan. His main areas of research interests include atmospheric pressure discharges, microwave plasmas, nanoparticle generation and electrohydrodynamics. He is the author and co-author of more than 20 scientific articles and 17 inventions.

Tung Thanh Bui received the B.S. degree in electrical engineering from Vietnam National University, Hanoi (VNUH) in 2004, and the M.E. and D.Eng. degrees in Science and Engineering from Ritsumeikan University, Shiga, Japan, in 2008 and 2011, respectively. From 2011 to 2015 he was a post-doctoral researcher with the 3D Integration System Group, Nanoelectronics Research Institute (NeRI), National Institute of Advanced Industrial Science and Technology (AIST), Tsukuba, Japan. Currently, he is an assistant professor at the Faculty of Electronics and Telecommunication (FET), University of Engineering and Technology (UET), Vietnam National University, Hanoi (VNUH). His current research interests are 3D system integration technology and MEMS based sensors, actuators and applications. He is the author and co-author of more than 60 scientific articles and 7 inventions.